

# Unlocking the Potential: Multi-task Deep Learning for Spaceborne Quantitative Monitoring of Fugitive Methane Plumes

Guoxin Si, Shiliang Fu, and Wei Yao *Senior Member, IEEE*

**Abstract**—Methane ( $CH_4$ ) is the second most prevalent greenhouse gas after carbon dioxide ( $CO_2$ ), with a short atmospheric lifetime of about 9.14 years. Reducing methane emissions could quickly mitigate global warming. A methane plume is a localized methane concentration. Methane emission monitoring involves three tasks: concentration inversion, plume segmentation, and emission rate estimation. The matched filter algorithm (e.g., Mag1c) for methane concentration inversion is sensitive to noise and reference signals. Research on methane plume segmentation is limited, often relying on subjective manual segmentation. Emission rate estimation typically uses the integrated mass enhancement (IME) algorithm, which depends on accurate meteorological measurements, limiting its applicability. Using PRISMA hyperspectral images from the WENT landfill in Hong Kong and the EnMAP hyperspectral dataset as a base map, we propose a deep learning framework for quantitative methane emission monitoring from hyperspectral images based on physical simulation. We simulate methane plumes using large eddy simulation (LES) and create various fugitive methane concentration maps using the radiative transfer equation (RTE). We further augment data to create a simulated EnMAP dataset ([https://github.com/Sigx093105/CH4\\_plume\\_dataset.git](https://github.com/Sigx093105/CH4_plume_dataset.git)). We train a U-Net for concentration inversion, a Mask R-CNN for plume segmentation, and a ResNet-50 for emission rate estimation. These deep networks outperform conventional algorithms in validation accuracy and generalize well on RPISAM data. We combine tasks into multi-task learning models: MTL-01 and MTL-02, which outperform single-task models. This research demonstrates multi-task deep learning for quantitative methane monitoring and can be extended to various methane monitoring tasks.

**Index Terms**—Methane plume, Hyperspectral remote sensing, Simulation, Multi-task deep learning.

## I. INTRODUCTION

Currently, landfills are still widely used around the world [33][57]. It is estimated that about 40-50% of the greenhouse gases emitted by landfills are methane [2]. Landfills account for approximately 5% of global methane emissions and are considered one of the largest anthropogenic sources of  $CH_4$  [45]. Furthermore, their contribution to atmospheric methane has been increasing since the beginning of the 21st century [5]. The emission of greenhouse gases, including methane, not only affects the surrounding ecological environment [24] but also has the potential to exacerbate extreme weather events in urban areas [55]. From 1960 to 2019, the

contribution of methane radiation stress accounted for 11% of total radiation stress, making it the second largest greenhouse gas after carbon dioxide. Compared to other main greenhouse gases, such as carbon dioxide and nitrogen oxides, methane exhibits a relatively short atmospheric life of approximately 9.14 years [5]. This implies that reducing methane emissions may have a quicker impact on alleviating global warming compared to reducing emissions of other greenhouse gases.

To detect emitted methane plumes, airborne data (AVIRIS-NG) is commonly utilized due to small-scale methane emission sources [10][11]. However, the advent of PRISMA, a new-generation hyperspectral satellite with a spatial resolution of 30m, has now made it feasible to retrieve spaceborne methane emissions [8]. The monitoring process for methane plumes can be divided into three tasks: (1) methane concentration inversion, (2) methane plume segmentation, and (3) estimation of single plume flux rates. For methane concentration inversion, current methods predominantly rely on differential optical absorption spectroscopy (DOAS) and matched filter techniques. DOAS, although computationally intensive, is typically used for small-scale inversion in scenarios where emission point sources are known [49][50]. On the other hand, matched filter algorithms are commonly applied for large-scale methane plume screening [11][48]. However, it is important to note that the accuracy of the matched filter algorithm is heavily based on the precise modeling of the target spectrum and background estimation [11][47].

Few studies have been conducted on methane plume segmentation, but it is crucial to accurately delineate single plumes, as it significantly determines the estimation accuracy of methane flux rate. Over the past few decades, a plethora of algorithms have been proposed for estimating point source emission rates. However, most of these algorithms require local wind speed data as auxiliary information, which is difficult to obtain due to the limited availability of meteorological observation stations[51] [28]. addressed this limitation by employing simulated plumes and deep learning techniques to estimate emission rates without the need for wind speed information, although the presented network could only estimate the emission rate of single-source plumes. In practical scenarios, it is often necessary to segment individual plumes from an image and estimate the emission rates separately.

Since the introduction of AlexNet in 2012, deep learning has witnessed rapid development and yielded remarkable results in various fields of remote sensing application[25][27][23]. The U-net deep learning architecture was initially designed

G.Si, S.Fu and W.Yao are with Department of Land Surveying and Geo-Informatics, The Hong Kong Polytechnic University, Hong Kong e-mail: (wei.yao@ieeee.org).

Manuscript received April 19, 2005; revised September 17, 2014.

for semantic segmentation tasks[40][36], but also exhibits enormous potential for regression[44]. We regard methane concentration inversion as pixel-by-pixel regression, so U-net can be used to complete the task. Additionally, Mask R-CNN has proven to be highly effective in a wide range of instance segmentation tasks [42] and should also be applicable to Methane plume segmentation. Moreover, ResNet addresses the issue of gradient vanishing, enabling deeper networks to improve feature extraction capabilities[19][43]. Many of the former works for emission rate estimation using shallow convolutional neural networks(CNN) have proven successfully to be realizable, but with moderate precision[26][18]. It is reasonable to apply ResNet to improve the emission rate estimation. And our goal is to leverage physically simulated plumes as training data for multi-task deep learning techniques to simultaneously perform methane concentration inversion, methane plume segmentation, and flux rate estimation in a unified approach.

In this article, we start by describing the foundational principles of the algorithms utilized in our study, including large-eddy simulation, radiation simulation, the methane plume concentration inversion algorithm, the methane plume segmentation algorithm (instance segmentation), and the plume emission rate estimation algorithm. Following this, we provide a detailed account of our experimental setup, which encompasses the research area, the collected data, and the procedures used to build our methane monitoring dataset. Lastly, we evaluate the performance of deep learning algorithms against traditional ones for the tasks of methane plume concentration inversion, methane plume segmentation (instance segmentation), and plume emission rate estimation. Furthermore, we present the two multi-task learning networks, MTL-01 and MTL-02, that we developed for these tasks. The major contributions of this paper are as follows:

1. We propose a physics-informed deep learning scheme for spaceborne retrieval of methane emissions based on data simulation using Large Eddy Simulation (LES), Radiative Transfer Equation (RTE), and data augmentation techniques.
2. We apply an instance segmentation algorithm to solve the problem of isolating and identifying methane emission sources by plume segmentation.
3. We show that the serialization of multiple sub-tasks for methane emission monitoring will lead to additional error accumulation, and designed a multi-task learning model to suppress the errors.

## II. METHOD

In this section, we present the principles of methane plume simulation, methane signal simulation, and methane concentration inversion. The two multi-task deep learning networks and relevant training mechanisms that we have designed are also presented.

### A. Simulation

The simulation operation consists of two parts: simulation of methane plume emission and simulation of EnMAP-like satellite images with methane plume signal. For methane

plume simulation, we utilized Large Eddy Simulation (LES), which is a computational fluid dynamics (CFD) method used to simulate turbulent phenomena in fluid flow[41]. It combines the advantages of Direct Numerical Simulation (DNS) and Reynolds-averaged Navier-Stokes equations (RANS) methods, aiming to accurately predict the statistical characteristics of turbulent flow[37][9]. The core of LES lies in filtering the flow field into large- and small-scale vortices through a filtering operation. This can be achieved by applying a low-pass filter to remove high-frequency small-scale vortices, while retaining the low-frequency large-scale vortices[9]. The filtered flow field equations form the basis of LES. The governing equations for LES are based on Reynolds-averaged Navier-Stokes equations (RANS)[14], which are solved to simulate motion and turbulent effects in the fluid [1]:

$$\frac{\partial \bar{u}_i}{\partial t} + \frac{\partial}{\partial x_j}(\bar{u}_i \bar{u}_j) = -\frac{1}{\rho} \frac{\partial \bar{p}}{\partial x_i} + \nu \frac{\partial^2 \bar{u}_i}{\partial x_j \partial x_j} - \frac{\partial}{\partial x_j}(\bar{u}'_i u'_j) \quad (1)$$

where  $\bar{u}_i$  is the time-average speed,  $t$  is the temporal change in fluid motion,  $x_i$  is the position of the fluid in a certain direction,  $\bar{p}$  is the average pressure of a fluid at a location,  $\rho$  is fluid density,  $\nu$  is kinematic viscosity[6], and  $\bar{u}'_i u'_j$  is the reynolds stress[29].

For simulation of EnMAP remote sensing images with methane plumes, we merged synthetic plume signals with real EnMAP remote sensing data[5]. First, plumes of different shapes, sizes, and concentrations were generated by simulation and assigned corresponding spectral characteristics based on physical radiation properties. Then we fused the synthetic plumes with real EnMAP remote sensing images to generate simulated images with realistic background textures and synthetic methane spectrum. Such simulated images are crucial for training and evaluating our algorithms, as they can simulate real observation scenarios under controlled experimental conditions[10]:

$$L(\lambda)' = L(\lambda) * T_{plume} \quad (2)$$

where  $L(\lambda)$  denotes the real EnMAP image background spectrum and methane signal,  $L(\lambda)'$  is the simulated spectrum,  $T_{plume}$  is the simulated methane absorption cross-section. And  $T_{plume}$  is generated by the summation of the radiative transfer equation (RTE), multiplied by the layered methane concentration and corresponding dry air density.

By combining these two steps, we can simulate methane plumes of various shapes, sizes, and concentrations and inject them into EnMAP data to generate simulated hyperspectral satellite images, which contain methane plume signal overlaid with a realistic scene background. This provides a solid foundation for our research and allows us to validate the performance and reliability of our methodology in real-world scenarios.

### B. Methane Concentration Inversion

Mag1c is a matched filter method that effectively aligns trace gas concentration path lengths by incorporating sparsity and reflectivity correction. Mag1c is also one of the most

advanced matched filter methods currently available and provides a mature and operational software interface[11]. The calculation formula for Mag1c is as follows[10]:

$$a = \frac{(L_i - u)^T C^{-1}(t(u))}{(t(u))^T C^{-1}(t(u))} \quad (3)$$

where  $a$  is methane concentration,  $L$  is radiation intensity,  $t(u)$  is mean radiation, and  $C$  is covariance matrix.

Methane concentration inversion in the Western New Territories (WENT) region was performed using PRISMA data and the mag1c method. The results of this inversion were evaluated against a deep learning model to validate its generalization capabilities. Considering the intricate distribution of land and sea areas in Hong Kong, as well as the challenging rugged terrain and dense urban construction, it can be expected that the surface conditions in the region significantly influence the results of methane concentration inversion. To address this, we utilize a K-means-based masking method to run Mag1c[13].

The U-net is a deep learning network characterized by an encoding-decoding structure and is primarily used for semantic segmentation tasks[40][36][56]. Typically, the input and output channels of the U-net are of equal size. However, to accommodate the requirements for the inversion of methane concentration, an additional layer of  $1 \times 1$  convolution is added after the U-net encoding-decoding structure[30], and the loss function is replaced for the regression task. The loss functions used include the mean squared error (MSE) and  $SmoothL_1$ :

$$loss_{mse} = \frac{1}{n} \sum_{i=1}^n (y_i - \hat{y}_i)^2 \quad (4)$$

$$loss_{SmoothL1} = \begin{cases} \frac{1}{2}(y - \hat{y})^2 & \text{if } |y - \hat{y}| < 1 \\ |y - \hat{y}| - \frac{1}{2} & \text{otherwise} \end{cases} \quad (5)$$

where  $y$  is the true label,  $\hat{y}$  is the predicted value,  $n$  is the number of samples, and  $|y - \hat{y}|$  represents the absolute difference between  $y$  and  $\hat{y}$ .

Prior to starting the training phase, various preprocessing techniques were applied to both the labels and images. In particular, we computed the mean and standard deviation of all non-zero pixel values in the labels to achieve normalization. Referring to the preprocessing methods of the DOAS algorithm, the subsequent formula was utilized to preprocess the images[53][35]:

$$I_{after} = \frac{\log(I_{before})}{10} \quad (6)$$

where  $I_{before}$  refers to the preprocessed image, and  $I_{after}$  represents the same image after preprocessing. Both EnMAP and PRISMA exhibit pixel values within the range of 0-10 after applying the logarithm, and dividing these values by 10 ensures that all preprocessed pixel values fall within the range of 0-1. This approach facilitates the generalization of the model across different sensors. The network is trained using two loss functions, MSE and SmoothL1, with an initial learning rate of 0.001. The learning rate is reduced by 75% every 10 epochs, totaling 200 epochs.

### C. Methane Plume Segmentation

Instance segmentation is a classical task in computer vision, and methane plume segmentation is essentially an instance segmentation task. Previous research work on methane plume segmentation is limited, and many studies are based on subjective segmentation criteria[16]. Some studies suggested using traditional algorithms for the segmentation of methane plumes, with contour tracking algorithms considered a good choice due to their efficiency and stability. On the other hand, there are many deep learning-based instance segmentation algorithms, among which Mask R-CNN is the most classical and widespread one[20]. It is a two-step instance segmentation algorithm that has been proven to achieve high performance in a large number of datasets for a wide range of applications. Although new instance segmentation algorithms are continuing to emerge, some of the algorithms sacrifice segmentation accuracy for real-time segmentation[46], which is not necessarily required for our case. Other algorithms may achieve higher instance segmentation accuracy[54], but require increasingly complex optimization processes during training, which is not cost-effective for our case. Therefore, we chose Mask R-CNN as the deep learning algorithm for methane plume segmentation and active contour algorithms as the traditional counterpart algorithm. Typically, Mask R-CNN takes three image channels as inputs, but we modified the input layer to allow flexible alteration between 1 or 41 input channels ( the methane distribution map has only one band, and EnMAP remains 41 bands after excluding water vapor and carbon dioxide sensitive bands[10]) to accommodate different segmentation requirements. We used the original loss function of Mask R-CNN:

$$L = L_{cls} + L_{box} + L_{mask} \quad (7)$$

where  $L$  is the total loss function,  $L_{cls}$  is the category loss function, which is based on the cross-entropy loss,  $L_{box}$  is the bounding box loss function, which is based on the  $SmoothL_1$  loss, and  $L_{mask}$  is the mask loss function, which typically uses the binary cross entropy:

$$L_{cls} = - \sum_{i=1}^N y_i \log(\hat{y}_i) \quad (8)$$

where  $y_i$  denotes the true label,  $\hat{y}_i$  is the probability predicted by the model, and  $N$  is the number of samples.

$$L_{box} = \sum_{i=1}^N smooth_{L1}(x_i - \hat{x}_i) \quad (9)$$

$$L_{box} = -IoU(b, \hat{b}) + \frac{\rho^2(b, \hat{b})}{c^2} \quad (10)$$

where  $b$  and  $\hat{b}$  respectively denote the ground truth bounding box and the predicted bounding box,  $IoU(b, \hat{b})$  indicates the intersection over the union between these two bounding boxes,  $\rho^2(b, \hat{b})$  is the Euclidean distance between the center points of two bounding boxes, and  $c$  is a hyperparameter typically set to 10.

#### D. Methane Emission Rate Estimation

There are two scenarios for estimating emission rates. The first scenario involves estimating the emission rates using training samples specifically collected for this purpose. The goal here is to evaluate the performance of the estimation algorithm under ideal conditions. The second scenario refers to the estimation of emission rates based on plume segmentation results (MTL-01), where the objective is to evaluate and improve the accuracy of the plume instance segmentation algorithms.

The emission rate of a methane plume is commonly estimated using the integrated mass enhancement (IME) mode[18]. This mode involves the following calculations:

$$Q = \frac{U_{eff} \cdot IME}{L} \quad (11)$$

where  $U_{eff}$  is the effective wind speed in  $m/s$ ,  $L$  is the plume length  $m$ ,  $IME$  refers to the integrated mass enhancement. And the calculations for  $U_{eff}$ ,  $L$ , and  $IME$  are as follows[51][18]:

$$U_{eff} = 0.34 \cdot U_{10} + 0.44 \quad (12)$$

where  $U_{10}$  is the wind speed at 10 meters.

$$L = \sqrt{A_M} \quad (13)$$

where  $\sqrt{A_M}$  is the area of a plume.

$$IME = k \sum_{i=1}^{n_p} \hat{\alpha}(i) \quad (14)$$

where  $n_p$  is the number of pixels in a plume,  $\hat{\alpha}(i)$  is the value of  $i$ th pixel, and  $k$  is a scale factor equal to  $5.155 \cdot 10^{-3} kg/ppb$ .

ResNet is a deep learning method that uses residual blocks, which enables the neural network to learn the residual map by effectively avoiding issues such as gradient vanishing and explosion[19]. ResNet is widely applied in various application fields, including image recognition, object detection, and speech processing, yielding impressive results[52][43]. We trained the ResNet-50 network on samples for emission rate to perform the flux rate estimation task. Subsequently, ResNet-50 was used as a pretrained network to validate the rationale of plume segmentation results and assist in optimizing the instance segmentation network.

#### E. Multi-task Learning I (MTL-01)

Experimental results indicated that the sequential prediction process involving Mask R-CNN followed by ResNet-50 led to substantial errors in emission rate estimation due to Mask R-CNN's false positives and false negatives (Fig. 9). While these errors could be tolerable in the context of plume segmentation, we have developed a multi-task network named MTL-01 to tackle this issue. This network concurrently trains both Mask R-CNN and ResNet-50.

Considering that the loss function of Mask R-CNN measures instance segmentation and does not consider error propagation, we design a serial network (MTL-01), which takes the

segmentation results of Mask R-CNN as input to ResNet-50 and calculates additional loss terms for back-propagation to assist in optimizing Mask R-CNN (Fig. 1). The ResNet-50 in the serial network is a pre-trained model, whose parameters are not updated. During the training process, the erroneous (over-)segmentation masks from Mask R-CNN are mainly categorized into two types. The first type is small false positive patches escaping from NMS(Non-Maximum Suppression) filtering[20], which were only found to slightly contribute to errors in subsequent emission rate estimation rather than main error source of the serial network. Simulation experiments indicate that the IME value of plumes is almost never below 300. Hence, we disregard false positive patches with IME values under 300 pixels, addressing this type of error using an object detection loss term. The second type of error consists of large false positive patches, often wrongly separated from overlapping plumes, causing substantial inaccuracies in emission rate estimation. To mitigate this, we introduce an additional loss term,  $loss_{ER}$ , for MTL-01. While  $loss_{ER}$  is still based on smoothL1, segmentation results with IME values below 300 pixels are excluded from its calculation. Missed masks are treated as having an emission rate estimate of 0 kg/h, and the loss is computed accordingly:

$$loss_{ER} = \begin{cases} loss_{SmoothL1}(y_i, \hat{y}_i) & \text{if } y_i \in TP \\ loss_{SmoothL1}(0, \hat{y}_i) & \text{if } y_i \in FP \end{cases} \quad (15)$$

In MTL-01, we consider the  $loss_{ER}$  term as a corrected loss term and assign it a coefficient lambda, while the original loss function of Mask R-CNN remains unchanged. Therefore, the loss function of MTL-01 is as follows:

$$loss_{MTL-01} = loss_{MaskR-CNN} + \lambda \cdot loss_{ER} \quad (16)$$

In this equation,  $loss_{MaskR-CNN}$  denotes the mask R-CNN loss function,  $loss_{ER}$  denotes the loss function of emission rate estimation, and  $\lambda$  is the coefficient. Based on our experiments, we found that  $\lambda = 0.1$  is optimal.

#### F. Multi-task Learning II (MTL-02)

The task of methane concentration inversion involves predicting pixel-level values from hyperspectral images, whereas methane plume segmentation focuses on extracting plume masks from the same type of images. Due to their similar structure and logical connection, employing multi-task learning models could potentially enhance accuracy for both methane concentration inversion and plume segmentation. Therefore, we developed a multi-task learning framework that combines U-net and Mask R-CNN architectures.

In MTL-02 (Fig. 1), the network architecture of Mask R-CNN remains unchanged, and the U-net decoding structure is connected to the mask R-CNN backbone network. Considering the output sizes of the stages in the ResNet-50 backbone network, we added an additional output to stage 0 of ResNet-50 to ensure that the size of the U-net decoding the result matches the input size, similar to LinkNet[58]. It should be noted that the deepest output of ResNet-50 is not involved in the construction of the U-net decoding structure

but only participates in the FCN[32] structure of Mask R-CNN. Furthermore, considering that there is a max-pooling layer between the two outputs of ResNet-50, which may lead to underfitting of the U-net decoding structure, we added an Atrous Spatial Pyramid Pooling (ASPP) layer composed of two dilated convolutions immediately after the U-net decoder, with dilation rates of 2 and 4.

ASPP (Atrous Spatial Pyramid Pooling)[7] is based on dilated convolutions and SPP (Spatial Pyramid Pooling)[21]. It is used to address the contradiction between reducing the feature map resolution as much as possible and capturing a large receptive field when extracting image features. ASPP uses dilated convolutions with different sampling rates to capture the context of an image at multiple scales. In ASPP, different dilated convolutions with different rates are applied to the input feature map and then merged. To enhance the

model’s receptive field, the output feature maps of the dilated convolution with different sampling rates are average-pooled.

For the loss function of  $MTL-02$ , we adopted the classical weighted average of individual loss functions for multiple tasks[4]:

$$loss_{MTL-02} = w_1 \cdot loss_{U-net} + w_2 \cdot loss_{MaskR-CNN} \quad (17)$$

where  $loss_{U-net}$  is the loss function of U-net,  $loss_{MaskR-CNN}$  is the loss function of Mask R-CNN, and  $w_1$  and  $w_2$  are the weights for respective loss components.

To determine the weights of the MTL-02 loss function, we used the Dynamic Weighted Average (DWA) algorithm[31], the idea of which is that different tasks have different levels of difficulty and learning speed. Instead of setting different learning rates for each task, it is better to dynamically adjust

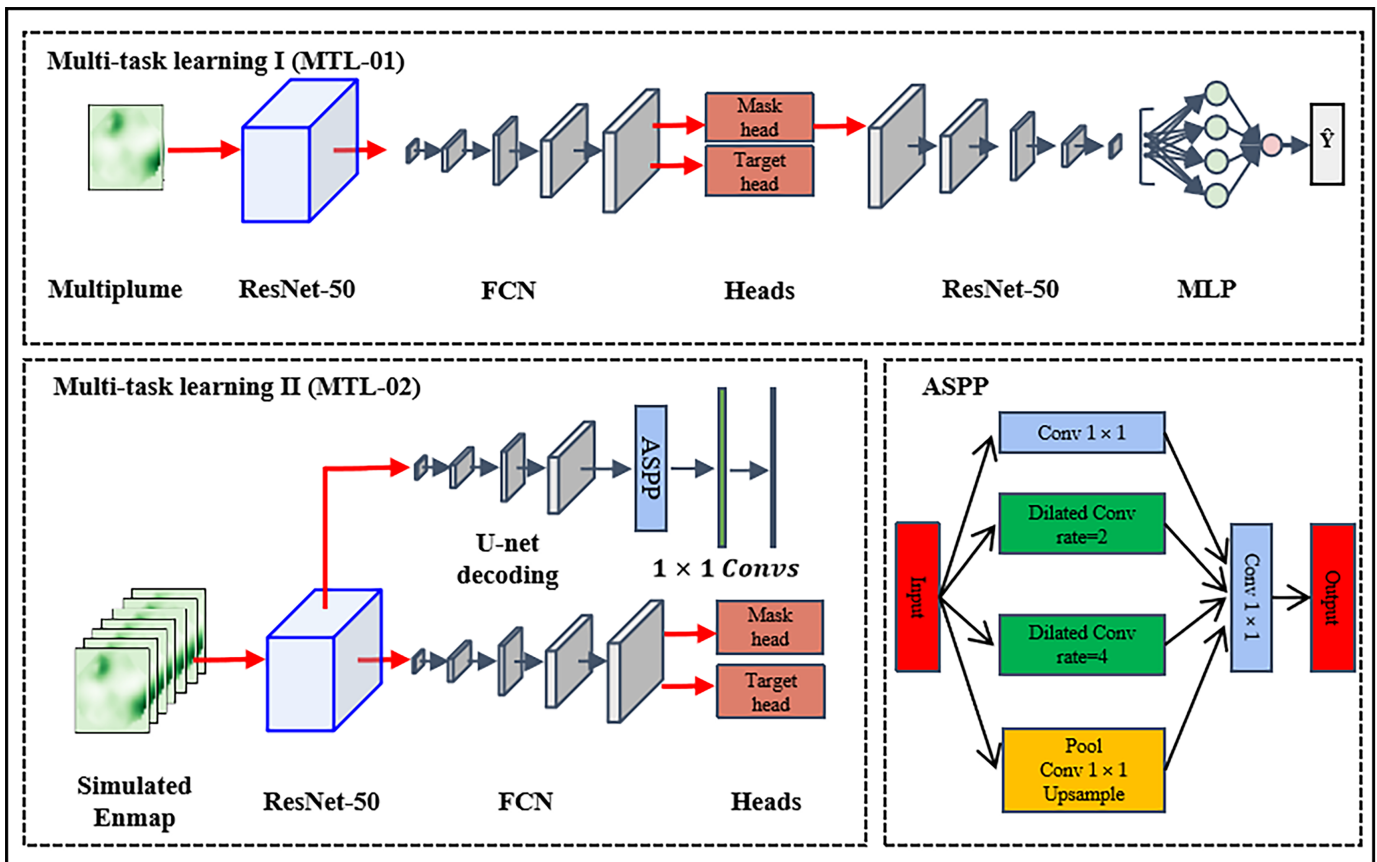


Fig. 1: The structure of the multi-task learning model

Multi-task learning I (MTL-01) is a sequential network that includes a Mask R-CNN (for plume segmentation) and a ResNet-50 (for plume emission rate estimation). The Mask R-CNN outputs segmented plumes, which are then processed by ResNet-50 in real time to compute the emission rate estimation loss. The overall loss for MTL-01 is the weighted sum of the individual losses from the two networks.

”Multiplume” refers to a methane concentration distribution map with multiple plumes, including noise. The ResNet-50 is a 50-layer residual network. FCN (Fully Convolutional Network) is a type of convolutional neural network that integrates low-level and high-level image semantic information through skip connections. ”Heads” in Mask R-CNN are responsible for object detection and mask extraction.

MLP stands for multi-layer perceptron. Multi-task learning II (MTL-02) is a network designed to detect methane concentration and methane plume boundaries concurrently. It is composed of a Mask R-CNN (for plume segmentation) and a U-Net (for methane concentration inversion) sharing a ResNet-50 feature extractor. While the decoding structure of the Mask R-CNN remains the same, the U-Net’s decoding structure is adapted to include four skip connections, followed by an ASPP structure and two 1x1 convolutions.

”Simulated EnMAP” refers to EnMAP data that include added methane plume signals. ASPP consists of a 1x1 convolution layer (used for channel reduction) and several parallel atrous convolution layers. The dilation rates of these atrous convolution layers are adjustable for extracting features at various scales. ”Conv 1x1” denotes a 1x1 convolution layer, ”Dilated Conv” indicates an atrous convolution layer, and ”Pool” represents a pooling layer.

the weights so that each task learns at a similar pace. In simple terms, tasks with faster loss reduction are assigned smaller weights, while tasks with slower loss reduction are assigned larger weights.

$$w_k(t) = \frac{K \cdot e^{-\frac{\lambda_k(t-1)}{T}}}{\sum_{i=1}^K e^{-\frac{\lambda_i(t-1)}{T}}} \quad (18)$$

$$\lambda_k(t-1) = \frac{L_k(t-1)}{L_k(t-2)} \quad (19)$$

where  $K$  is the number of tasks,  $\lambda_k(t-1)$  denotes the rate of loss reduction for the  $k$ -th task during the  $(t-1)$ -th training iteration, and  $L_k(t-2)$  represents the loss for the  $k$ -th task during the  $(t-2)$ -th training iteration. When  $T$  is a constant,  $T = 1$  indicates that  $w$  is equal to the result of softmax; However, as  $T$  increases significantly,  $w$  approaches 1, leading to equal loss weights for all tasks.

### III. EXPERIMENTS

#### A. Research areas and data

1) *Research areas*: Situated in the southern part of China, Hong Kong is predominantly marked by hilly terrain. The region, which is highly urbanized, experiences a humid and rainy climate, with an average annual precipitation exceeding 2000 millimeters. Within Hong Kong, there are two key landfills: the Western New Territories (WENT) Landfill and the North East New Territories (NENT) Landfill. Since most of the PRISMA images were obtained from the WENT region, our generalization verification is mainly concentrated in this area. The Tuen Mun landfill (Fig. 2), which spans approximately 27 hectares, is located in the southwest of the Tuen Mun district near Shenzhen Bay. It is one of the limited waste disposal sites sanctioned by the government in the Hong Kong Special Administrative Region and primarily receives municipal solid waste from various areas, including Hong Kong Island, Kowloon, and New Territories.

2) *Hyperspectral Data*: The PRISMA satellite was launched on March 22nd, 2019, and offers hyperspectral images of global coverage with a spatial resolution of 30 m. The spectral smile is less than 5 nm, the spectral resolution is better than 12 nm in a spectral range of 400-2500 nm (VNIR and SWIR regions) [8], and datasets are open-access. We have collected several PRISMA images of WENT, which are: 20220102, 20220119, 20220914, 20230217, 20230301, 20230307, 20230416. These raw images will be used to verify the generalizability of deep learning models[50][10].

The EnMAP satellite was launched on March 22nd, 2019, and provides hyperspectral images with global coverage and a spatial resolution of 30 m. The spectral smile is less than 5 nm, and the spectral resolution is better than 12 nm within a spectral range of 400-2500 nm (VNIR and SWIR regions). The EnMAP dataset is obtained from the publicly available atmospheric correction dataset[12], which includes 11,000 images in total. These images are stored in geotiff format, with a resolution of 30m × 30m, and include a total of 224 spectral bands. Initially, we retrieved the data matrices and corresponding metadata from the geotiff files.

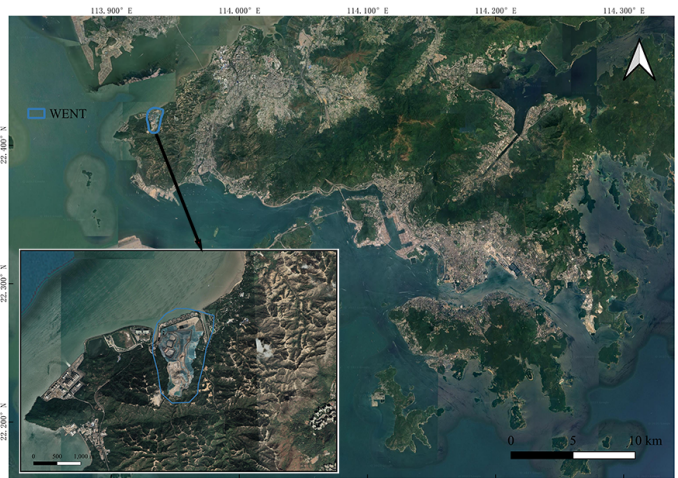


Fig. 2: Research area

The study site is the WENT landfill found in the Tuen Mun District of the Hong Kong Special Administrative Region. WENT is located on a slope near Shenzhen Bay, as shown by the blue box on the map.

We then removed the water vapor and carbon dioxide sensitive bands, leaving 41 bands. Following this, we resampled the extracted 41-band data to a size of 256 × 256 pixels using the xx interpolation method. During this process, no fitting is performed on the spectral curves. This effectively increases the area coverage of ground features by four times while maintaining the original spatial resolution of 30m.

#### B. Generation of snapshots for plumes of different emission rates and wind speeds

Our simulated plumes were generated using palm software[38][34], using the average atmospheric pressure at sea level in Hong Kong (0.96 hPa) and a temperature of 296K. A specialized smog mode was implemented, including a methane dispersion feature, to simulate the diffusion of methane point sources within the troposphere from 0 to 10,000 meters. We defined four gradients for the methane point source emission rate: 500kg/h, 1000kg/h, 1500kg/h, and 2000kg/h. The wind direction was set from west to east, with wind speed gradients of 1m/s, 2m/s, 3m/s, 4m/s, 5m/s, 6m/s, 7m/s, 8m/s, 9m/s, and 10m/s (Fig. 3). For each wind speed gradient, the methane point source emission rate gradients were simulated in sequence. The simulation period covered 0 to 2.5 hours, with snapshots taken at 30-second intervals from 1 to 2.5 hours, resulting in a total of 7200 plume snapshots. Among them, the simulated plume emission data with wind speeds of 2m/s, and 10m/s were used to create the validation dataset, the simulated plume emission data with wind speeds of 1m/s, and 9m/s were used to create the test dataset, while the remaining plume emission data were used to create the training dataset.

#### C. Generation of multi-task learning datasets

The dataset we are going to create consists of three subsets: inversion dataset, segmentation dataset, and emission rate dataset. Each subset comprises three groups of data,

namely Train, Val, and Test, which are respectively used for training, validation, and testing. Each group of data contains several samples, and each sample includes an image and its corresponding label. We assign plume snapshots of different wind speed gradients to Train, Val, and Test. The base map is also randomly divided into three groups and allocated to Train, Val, and Test accordingly. The creation process of a single sample group is as follows(Fig. 4):

By taking a snapshot of a plume and averaging the methane concentrations at different heights, a 2D single plume with an emission rate of  $m$  kg/h is obtained. Multiplying all pixel values of the 2D plume by a factor of  $a$  results in a modified emission rate of  $m \cdot a$  kg/h, which serves as the label for the sample in the emission rate dataset. To ensure the diversity of plumes, we randomly generate a threshold value between 0.05 and 0.10, and pixels in the 2D plume that are below this threshold are set to zero. Finally, a rotation enhancement of  $-170^\circ$  to  $170^\circ$  is applied to the 2D plume, serving as the image counterpart to the label in the emission rate dataset sample. Plume segmentation is an instance segmentation task. To begin with, we create an empty  $256 \times 256$  image filled with zeros. Then, we select  $N$  images from the emission rate dataset (where  $N \leq 3$  and  $N$  can be 0), and superimpose them randomly onto the all-zero image to obtain a multi-plume image. Simultaneously, we identify the boundaries of each plume and assign corresponding labels to the segmentation dataset. If  $N = 0$ , the dataset will have no labels. Finally, we randomly generate  $256 \times 256$  Gaussian white noise and add it to the multi-plume image[28][15], which serves as the image for the segmentation dataset. Furthermore, the overlap ratio of the two plumes' could not exceed 15%:

$$Overlapratio(A, B) = \frac{\sum_{x_i \in A \cap B} x_i}{\sum_{x_i \in A \cup B} x_i} \quad (20)$$

where A,B represent two 2D plumes,  $x_i$  is the pixel value in the plume.

The inversion data are derived from the multi-plume images generated during the creation of the segmentation dataset, where these multi-plume images are used as labels for the inversion dataset samples. Initially, a multi-plume image is

obtained and checked for emptiness. If found empty, a random EnMAP image is selected as the sample image. Conversely, if the multi-plume image is not empty, methane transmission spectra corresponding to each pixel value are constructed column by column. For columns entirely composed of zeros, the transmission spectrum is set to a  $256 \times 1 \times 41$  matrix with all elements equal to 1. For columns with non-zero elements, an optical depth matrix of size  $256 \times 1 \times K$  (where  $K$  is the number of elements in the absorption cross-section data) is generated using the method described in Section II.A. The negative logarithm of the pixel values in the optical depth matrix is then taken to derive the original transmittance matrix.

Initially, the central wavelengths and half-bandwidths of the 41 EnMAP bands are obtained to build the spectral response function (SRF)[17][3]. Subsequently, the SRF is applied to perform normalized convolution along the  $K$  dimension of the original transmittance matrix, producing a  $256 \times 1 \times 41$  'column' transmission spectrum matrix. After each column of the non-empty multi-plume image is processed, all the transmission spectrum matrices are concatenated in their original column sequence to create a  $256 \times 256 \times 41$  transmission spectrum matrix.

Finally, the transmission spectrum matrix is combined with random EnMAP data via the Hadamard product to generate the image for the non-empty multi-plume. It is crucial to highlight that, because the simulated methane plumes are concentrated below an altitude of 3000 meters, we use the average temperature and atmospheric pressure of Hong Kong to compute the methane absorption cross-section and calculate the optical depth using the mean atmospheric density from 0 to 3000 meters. Although this approach might sacrifice some spectral simulation precision, the trade-off is considered acceptable due to the significant computational burden involved in generating the inversion dataset. The entire code for creating the inversion dataset is written in PyTorch and runs on an NVIDIA GeForce RTX 3060 GPU.

#### D. Accuracy Assessment

1) *Regression Task*: Both inversion of methane concentration and estimation of emission rate are integral to the

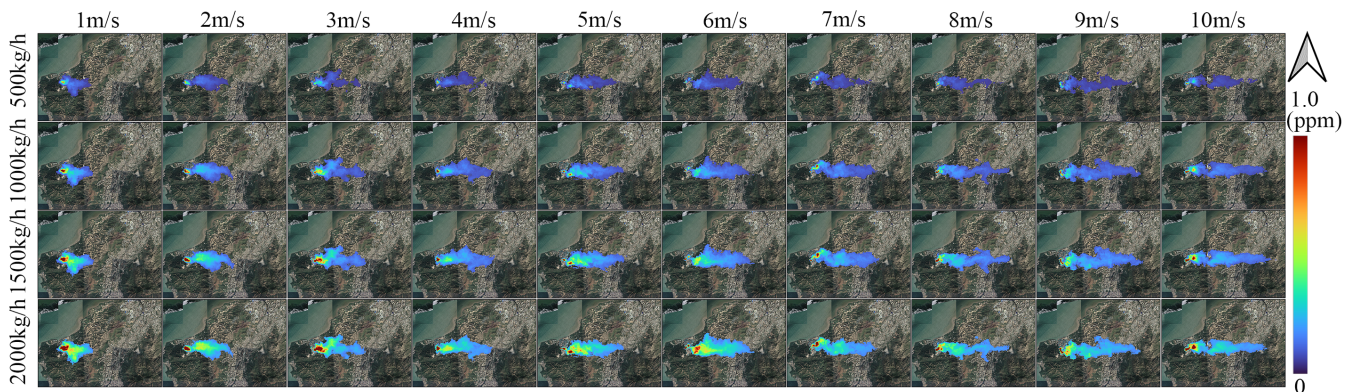


Fig. 3: Snapshot of a methane plume simulated by the Palm software

This figure illustrates the methane plume at various emission rates and wind speeds, modeled with the Palm software. Each image was taken 180 minutes post-emission initiation, with simulation parameters specified in Section II.B.

regression mission. Hence, to evaluate accuracy, we employed the RMSE and MAE metrics.

$$RMSE = \sqrt{\frac{1}{n} \sum_{i=1}^n (y_i - \hat{y}_i)^2} \quad (21)$$

$$MAE = \frac{1}{n} \sum_{i=1}^n |y_i - \hat{y}_i| \quad (22)$$

where  $y$  is the ground truth value,  $\hat{y}$  is the predicted value, and  $n$  is the number of samples.

2) *Segmentation Task*: We used average precision (AP) to measure the accuracy of the methane plume segmentation task. The formula for calculating AP is as follows[22]:

$$Precision = \frac{TP}{TP + FP} \quad (23)$$

1. Set a threshold and determine the number of  $TP$ ,  $FP$ ,  $TN$ , and  $FN$  according to the threshold.

$TP$ : True positive, the number of positive samples correctly classified as positive.

$FP$ : False positive, the number of negative samples falsely classified as positive.

$TN$ : True negative, the number of negative samples correctly classified as negative.

$FN$ : False negative, the number of positive samples falsely classified as negative.

2. Calculate precision by dividing the number of true positives by the sum of the number of true positives and false positives.

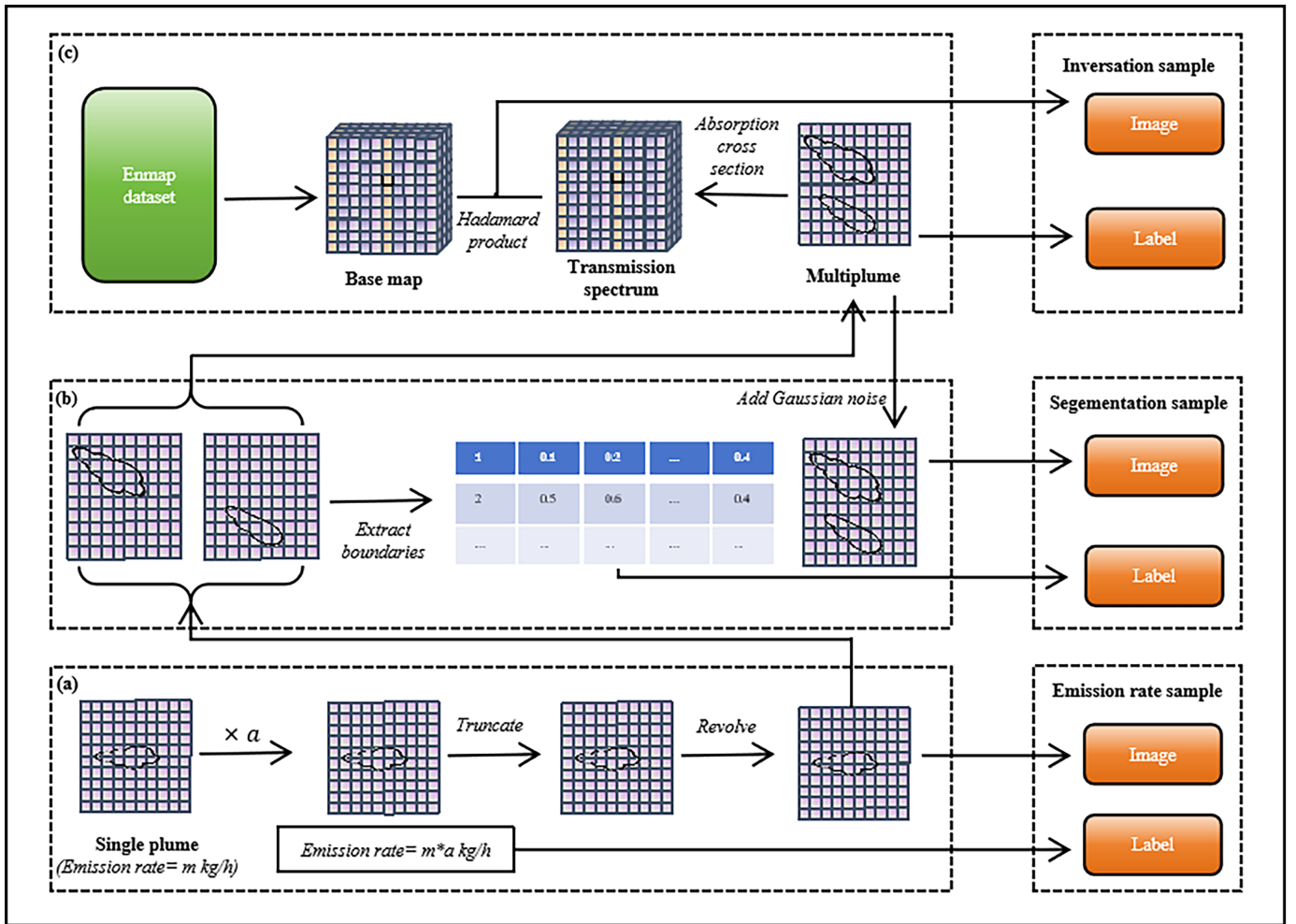


Fig. 4: Generation process of training samples

The training dataset is composed of three types of samples: Emission Rate Sample, Segmentation Sample, and Inversion Sample. The training dataset is formed by a large number of these samples. (a) The snapshot of the plume simulated by palm is scaled (including the emission rate), and the concentration values are thresholded (pixels below a certain threshold are set to 0). Random rotation within the range of  $-170^\circ$  to  $170^\circ$  is applied to generate a single enhanced plume, which represents the Emission Rate Sample image, and the scaled emission rate is used as its label. (b) Up to  $N$  ( $N \leq 3$ ) plumes from step (a) are combined at random positions (the overlap between two plumes must not exceed 70%) to create a multi-plume image. Noise from maglc inversion results is added to the multi-plume image to form the Segmentation Sample image, with the boundary of each plume being noted as the label. (c) Using the process from (a), a transmission spectrum matrix matching the dimensions of the EnMAP base map is produced based on the multi-plume image from (b). The simulated EnMAP image is then created by applying the Hadamard product of the transmission spectrum matrix and the EnMAP base map, serving as the Inversion Sample image. The multi-plume image acts as the label for the Inversion Sample.

3. Calculate the recall by dividing the number of true positives by the sum of the number of true positives and false negatives.

$$Recall = \frac{TP}{TP + FN} \quad (24)$$

4. Repeat this process for different thresholds to obtain a set of precision and recall values.

5. Calculate the AP value:

$$AP = \sum_{i=1}^{n-1} (R_{i+1} - R_i) P_{inter}(R_i + 1) \quad (25)$$

where  $(R_{i+1} - R_i)$  is the length of recall interval, and  $P_{inter}(R_i + 1)$  is the interpolated precision at recall  $R_i + 1$ . The AP value is calculated by summing up all interpolated precision values weighted by the lengths of recall intervals between adjacent recalls.

#### IV. RESULTS AND DISCUSSIONS

##### A. Simulation

To verify the accuracy of the simulated plumes, we consulted relevant studies[16]. The integrated methane emission (IME) values for a typical methane plume should exhibit a linear relationship with its emission rate. We computed the IME values for all 2D plume snapshots, plotted them against their respective emission rates in a scatter plot, and fitted a linear curve, from which we obtained the coefficient of determination. The findings show that the coefficient of determination for the linear curve was 0.88 (Fig. 5), indicating a linear correlation between the IME values and emission rates of these 2D plume snapshots. Therefore, we can conclude that the quality of simulated methane plumes is reasonable to a large extent.

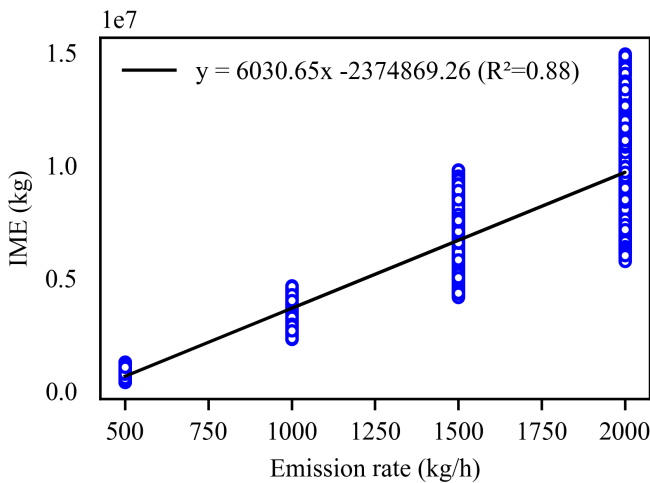


Fig. 5: Correlation between emission rates and simulated plume dataset IME values.

We calculated all 2D plume snapshots simulated by palm software and their IME values. We plotted a scatter diagram of IME values of plume snapshots and their corresponding emission rates and fitted a linear curve. The results show that there is a high correlation between IME values and emission rates of these plume snapshots.

We employ simulation techniques to create EnMAP datasets with plume signals. Despite the fact that the production process adheres to theoretical foundations, the physical model remains a simplified version of actual conditions. Thus, it is essential to confirm the validity of incorporating plume signals into the EnMAP base map. In the absence of actual labels, we utilize an end-to-end method to confirm the simulated EnMAP images. Firstly, a random 2D plume snapshot is captured, and a transmittance matrix is constructed following the procedure detailed in Section II. Next, a random EnMAP base map is chosen and combined with the transmittance matrix using the Hadamard product to generate a simulated EnMAP image. Following this, the Mag1c tool is employed to extract the methane concentration distribution map from the simulated EnMAP image. Finally, we compare the 2D plume snapshot to the methane concentration distribution map. If their methane concentration distributions match closely, the plume signal incorporation process can be deemed valid. In Fig. 6, the left image shows a 2D plume snapshot, whereas the right image presents the methane concentration distribution map derived by Mag1c from the relevant EnMAP data. It is notable that the right image contains some additional noise compared to the left, but the primary features are quite similar, thereby validating the plume signal incorporation process.

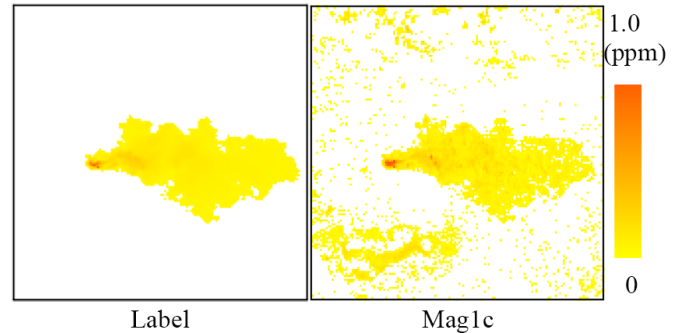


Fig. 6: The results of end-to-end verification for simulation. Due to the absence of the ground truth value of methane concentration, we verify it through an end-to-end method: comparing the methane plume extracted from the simulated EnMAP image using mag1c with the methane plume added to the EnMAP base map. The results show that the methane plume extracted by mag1c closely resembles the plume incorporated into the EnMAP base map, indicating that the addition of the plume signal is appropriate.

##### B. Methane Concentration Inversion

Each model was assessed on the test dataset for methane concentration inversion (see Table I). The results from the validation suggest that the deep learning model consistently surpasses Mag1c in inversion accuracy, with U-net employing MSE yielding better precision than with SmoothL1. Reviewing the comprehensive validation results, it can be deduced that the U-net network exhibits superior predictive capabilities compared to Mag1c. However, the validation using simulated data may introduce some bias. To address this, we further evaluated U-net’s generalization performance using PRISMA data from WENT.

TABLE I: VALIDATION RESULTS OF METHANE CONCENTRATION INVERSION

Methods	RMSE/ <i>ppm</i>	MAE/ <i>ppm</i>
Mag1c	0.5377	0.1392
U-net + Smooth $L_1$ loss	0.1208	0.0225
U-net + MSE loss	0.0926	<b>0.0159</b>
MTL-02	<b>0.0790</b>	0.0196

Since PRISMA and EnMAP have 49 and 41 bands remaining after removing the sensitive bands for water vapor and carbon dioxide, we first resampled the PRISMA data into 41 bands in the spectral direction, referring to the center wavelengths of the 41 bands of EnMAP that participate in prediction. Then we used the trained U-net to invert the methane plume in this region and compared it with the Mag1c inversion results based on 49 PRISMA bands. As shown in Fig. 7, there are three representative inversion visualization results. It can be seen that in some data, the inversion results of U-net and Mag1c are consistent, while there are some discrepancies in the inversion results of the two methods in some data. Due to the absence of a true concentration value for the methane plume column in the WENT region, it is impossible to ascertain which method yields the most accurate inversion results. We explore possible reasons for the disparities in the inversion outcomes between the two approaches: 1. The WENT region is uneven and near the ocean, and the complexity of the noise distribution in the collected PRISMA data affects the two methods differently. 2. The resampling process of the PRISMA data results in some loss of plume information, causing disparities in the inversion results of U-net and Mag1c. 3. There is a limited number of EnMAP base maps used for U-net training available in rugged areas, leading U-net to likely predict methane column concentrations based on smoother terrains.

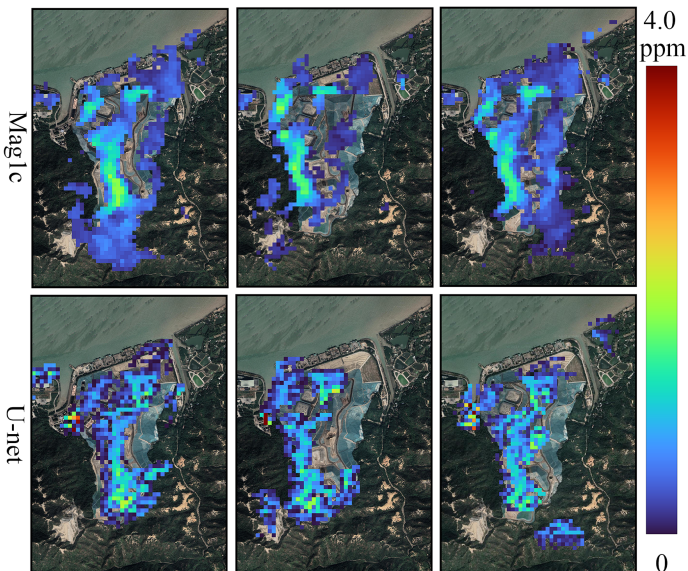


Fig. 7: Comparison of generalization results between U-net and Mag1c on real data.

Sample illustrations of U-net’s generalization performance on PRISMA..

### C. Methane Plume Segmentation

We trained the Mask R-CNN model using two versions of the plume segmentation dataset described in Section II.C. One version used simulated hyperspectral images as input (hyperspectral image), while the other version used methane plume distribution maps (single). However, the labels for both versions of the dataset were identical. Similarly, we separately validated the models using validation sets corresponding to two versions of the dataset with identical labels. Note that the Active Contour method was only validated using single methane plume maps as input, since it is an unsupervised image segmentation method that needs to explicitly relate pixel values to task-dependent physical property. The results showed that the Mask R-CNN model achieved a higher precision than Active Contour (Table II). Nonetheless, when evaluating the AP metric at  $AP_{95}$ , the Active Contour method surpassed Mask R-CNN in accuracy, suggesting that Active Contour excels at isolating individual plume masks. Despite this, Active Contour exhibits lower overall performance compared to Mask R-CNN due to its inability to effectively distinguish overlapping plumes and its propensity to produce small extraneous segmented areas.

TABLE II: VALIDATION RESULTS OF METHANE PLUME SEGEMENTATION

Models	$AP_{50}$	$AP_{75}$	$AP_{95}$	$AP_{50:95}$
Active Contour	42.03	39.04	<b>9.35</b>	34.96
MTL-01	<b>84.06</b>	<b>79.93</b>	0.00	<b>64.74</b>
Mask R-CNN single	82.58	76.73	0.00	61.84
Mask R-CNN hyper	29.28	14.70	0.00	15.07
MTL-02	35.21	15.44	0.00	17.14

Both versions of Mask R-CNN demonstrate superior precision in extracting the plume mask from the methane plume distribution map compared to extracting it directly from hyperspectral images. This is primarily due to two factors: first, the EnMAP data, produced through a two-step simulation process, inherently contain more errors than the one-step simulation method. Second, extraction of the EnMAP plume mask involves both inversion and segmentation steps, which increases the likelihood of inaccuracies compared to direct extraction from the methane plume distribution map. Regarding the “single” Mask R-CNN, despite its capability to efficiently segment overlapping plumes, its segmentation outcome still exhibits some errors (Fig. 8). These errors can be generally categorized as follows: 1. If a plume is divided into two sections, the single Mask R-CNN may incorrectly segment it into two separate plumes. 2. For overlapping plumes, the single Mask R-CNN may generate redundant or duplicate segmentations.

To evaluate the Mask R-CNN model’s ability to generalize to real-world contexts, we utilized mag1c to reverse-engineer methane concentration maps from various PRISMA images within the WENT area. Subsequently, both Active Contour and Mask R-CNN were applied to delineate methane plumes. The blue boxes in Fig. 9 denote these identified plumes. It is evident that Active Contour maps all connected pixel regions, whereas Mask R-CNN typically highlights funnel-shaped pixel

regions, indicating some resistance to noise. Despite this, both methods identified a comparable number of methane plumes. We acknowledge the absence of precise data on the exact count of methane emission sources (or plumes) in the WNET area. Nevertheless, visual inspection reveals that both techniques detected the major plumes and overlooked several smaller ones on the right. This omission could be attributed to the rugged coastal terrain of the WENT region, where plume dispersion is influenced by intricate factors like topography and sea-land breeze dynamics, resulting in more complex plume formations.

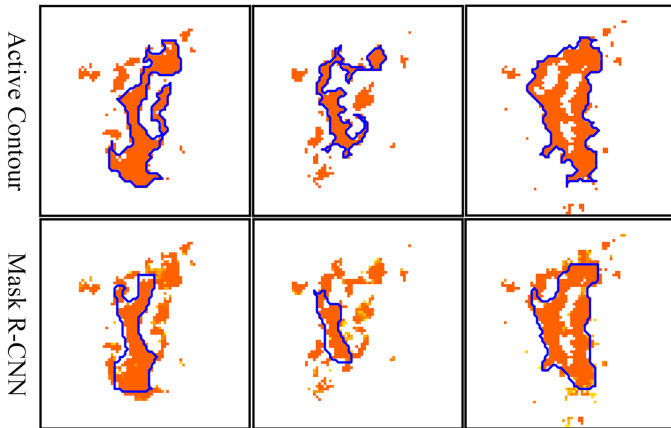


Fig. 9: Comparison of generalization results of different methods on real plume images

To assess the generalizability of the Mask R-CNN model on real-world data, we employed `mag1c` to invert the methane concentration map derived from multiple PRISMA datasets in the WENT region. Subsequently, we used both Active Contour and Mask R-CNN to extract the methane plume. The area marked by the blue line in the figure indicates the extracted methane plume. It is evident that Active Contour aims to extract all connected pixel regions extensively, while Mask R-CNN focuses on pixel regions with a funnel-shaped distribution. Nonetheless, the overall count of methane plumes identified by both methods is comparable.

#### D. Estimation of Methane Emission Rate

We trained ResNet-50 and AlexNet for emission rate estimation using the training dataset and verified the accuracy of the model estimation in the corresponding test set (Table III). The results show that ResNet-50 outperforms the IME algorithm in the validation set. The emission rate estimation accuracy of AlexNet is slightly higher than that of the IME algorithm, but lower than ResNet-50. This aligns with the relevant experience in the field of deep learning, where a deeper network means that each layer of the network can perform less complex tasks, thus obtaining more nonlinear expressive capabilities, learning more complex mappings[39], and enhancing the generalization performance and robustness of the network.

TABLE III: VALIDATION RESULTS OF EMISSION RATE ESTIMATION OF SINGLE NETWORKS

Methods	RMSE/ $kg * h^{-1}$	MAE/ $kg * h^{-1}$
IME	187.47	142.05
AlexNet + MSE loss	177.31	141.03
ResNet + MSE loss	<b>126.93</b>	<b>96.09</b>

To assess the ResNet-50's ability to generalize to real-world data, we employed `Mag1c` to invert methane concentration distribution maps derived from RPISMA data in the WENT region and manually identified 28 methane plumes. We estimated their emission rates using both the IME method and the pre-trained ResNet-50 model, constructed scatter plots, and performed linear curve fitting. As shown in Fig. 10, the scatter plot illustrates that the majority of points are aligned closely to a straight line, indicating that the predictions from both approaches are typically in good agreement with the real-world dataset. However, it is also apparent that the ResNet-50 model shows a tendency to saturate in areas with lower emission rates.

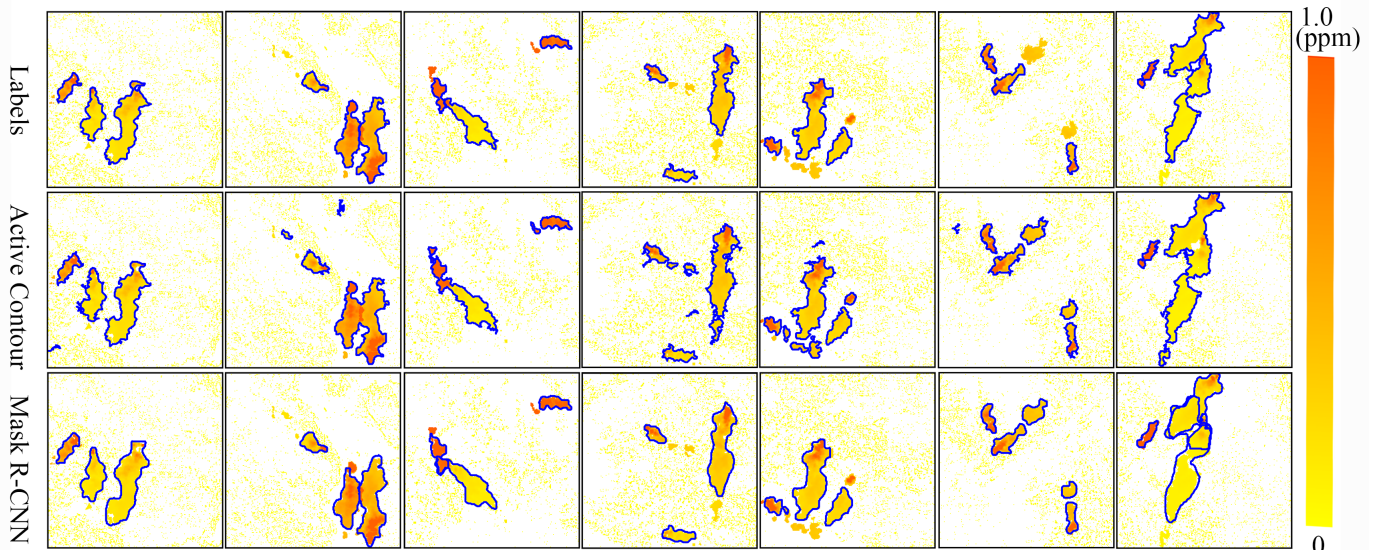


Fig. 8: Segmentation results of various methods on the test dataset

The region outlined by the blue border in the figure shows the segmentations of the methane plume produced by different methods.

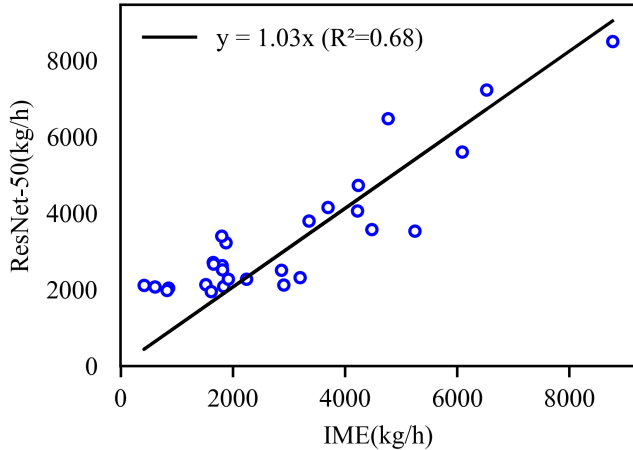


Fig. 10: Comparison of generalization results between ResNet-50 and IME on real data

We manually extracted 28 methane plumes from the inversion results of PRISMA’s WENT region and predicted their emission rates using the IME method and the trained ResNet-50 model separately. The prediction results are shown in the figure above. Both methods yielded comparable results. However, it can also be observed that ResNet-50 shows some saturation in regions with low emission rates.

E. Serial Network

While individual models demonstrated high accuracy for each specific task, the efficacy of serializing multi-network models still warrants further examination. Initially, we combined Mask R-CNN and ResNet-50 to handle the tasks of segmenting methane plumes from concentration maps and estimating their emission rates. We assessed the accuracy of these emission rate estimates on the validation set under three scenarios: 1. For true positive segmented plumes, we used pre-trained ResNet-50 to estimate emission rates and compared them with the label’s emission rates. 2. For false positive segmented plumes, we similarly used ResNet-50 to estimate their emission rates and compared them against 0 kg/h. 3. For misdetected plumes, we assumed their emission rate estimates to be 0 kg/h and compared these estimates with the corresponding labels. Ultimately, RMSE and MAE between all predicted emission rates and label values were calculated (Table IV). The results indicated that the accuracy of emission rate estimation using Mask R-CNN + ResNet-50 was significantly lower than using ResNet-50 for single-task emission rate estimation. It indicates that the serialization of Mask R-CNN and ResNet-50 could introduce additional errors in overall performance of methane flux rate estimation.

TABLE IV: VALIDATION RESULTS OF EMISSION RATE ESTIMATION OF SERIAL NETWORKS

Methods	RMSE/kg * h <sup>-1</sup>	MAE/kg * h <sup>-1</sup>
ResNet-50 + MSE loss	<b>126.93</b>	<b>96.09</b>
Mask R-CNN+ResNet <i>plume</i> <sub>300</sub>	1157.45	859.56
MTL-01	1038.30	788.31

To further explore the additional error sources, we selected

the segmented plumes with large errors (e.g. greater than 500 kg/h). The results revealed two sources of additional errors: 1. Errors caused by small patches that actually contain only noises; 2. Errors caused by false positive patches.

We also studied the distribution of small noise patches and found that most are characterized by a mask size of smaller than 300 pixels, whereas the real plume mask size is rarely smaller than 300 pixels. Therefore, we removed the segmented masks whose sizes are smaller than 300 pixels and revalidate the accuracy of Mask R-CNN + ResNet-50 for emission rate estimation.

F. Multi-task Learning I (MTL-01)

We trained the MTL – 01 network and after 30 epochs of training, MTL – 01 achieved higher accuracy in the plume segmentation problem compared to training Mask R-CNN alone. Consequently, the loss in the estimation of the emission rate of multiple methane flows was also smaller than in the case of serialization of *Mask R – CNN* and *ResNet – 50*. Furthermore, we simulated a smaller dataset to train the networks using the two approaches and MTL–01 exhibited even greater accuracy compared to serializing *Mask R – CNN* and MTL – 01.

We can observe that the segmentation of additional plumes is suppressed(Fig. 9), thereby reducing the estimated emission rate. MTL – 01 tends to segment the main parts of the jet stream, ignoring some smaller tail parts. This has brought improvements to both the plume segmentation task and the estimation of the emission rate(Table II, Table IV).

G. Multi-task Learning II (MTL-02)

We trained the MTL-02 model, which converged after 30 epochs, with both the loss function values and the validation accuracy values rapidly decreasing. Ultimately, MTL-02 achieved slightly higher accuracy in methane concentration inversion compared to U-net(Table I), and higher accuracy in plume segmentation compared to Hyper Mask R-CNN(Table II). This confirms the viewpoint that multi-task learning could improve the convergence speed and fitting accuracy of the model. This may be attributed to the shared information among multiple types of labels.

H. Limitations

Monitoring methane plumes is an intricate issue, and the current research in this domain is neither thoroughly explored nor systematic. Our proposed method also has some constraints: 1. The shapes of the simulated plumes we used mostly adhere to a standard Gaussian model, which represents an ideal scenario. However, in reality, methane emissions from point sources are influenced by a variety of factors like topography and humidity, leading to non-Gaussian plumes. Whether our method applies to non-Gaussian plumes remains an open question; 2. The maximum overlap ratio of the plumes we examined is 15%. However, naturally, many methane emission sources are situated close to each other, and the overlap ratio of two plumes can be significantly

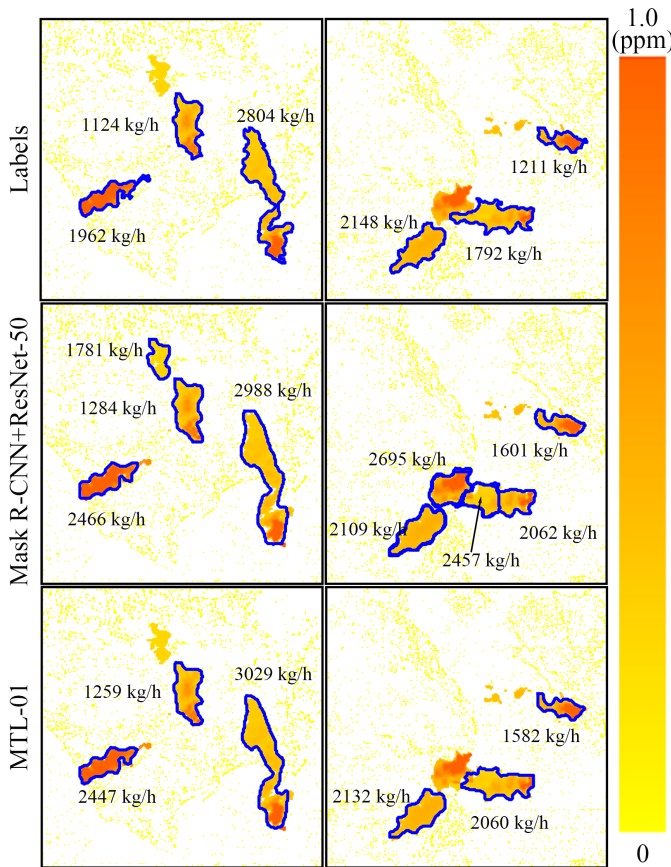


Fig. 11: Comparison of serial networks and multi-task learning I (MTL-01).

higher than 15%. In such scenarios, even though we can generate highly overlapped methane plumes, it is challenging to provide precise training labels, necessitating the exploration of point-based semi-supervised learning techniques to achieve reasonable segmentation outcomes for these highly overlapped plumes; 3. The acquisition of hyperspectral satellite imagery is significantly affected by weather conditions, and hyperspectral image data sources are scarce in low-latitude coastal regions. Hence, a solution relying solely on hyperspectral images may not fulfill high-frequency monitoring needs. It is essential to devise an ensemble estimation method based on multiple data sources.

## V. CONCLUSION

Currently, there are high uncertainties in fugitive methane emission monitoring methods using satellite imaging spectrometers. We have developed a demonstrative approach that utilizes deep learning models and simulated hyperspectral images for methane concentration inversion, plume segmentation, and emission rate estimation in landfills. Specifically, we employed U-net for methane concentration inversion, achieving higher accuracy and reduced noise compared to mag1c. We utilized Mask R-CNN for plume segmentation, avoiding subjectivity in the segmentation process. For methane plume emission rate estimation, ResNet-50 is employed to overcome

the reliance on wind speed observations. We also discussed the additional errors of emission rate estimation introduced by serial networks and addressed this issue by training a multi-task model (MTL-01) to suppress the errors and improve the precision of plume segmentation. Additionally, a multi-task model (MTL-02) that simultaneously performs methane concentration inversion and plume segmentation is proposed, achieving higher validation accuracy than individual single-task models. Finally, we also indicated the limitations of the current approach, highlighting the need for future research into highly overlapped plumes, non-Gaussian plumes, and the synthesis of multi-source data for inversion.

## ACKNOWLEDGMENT

The work described in this paper was substantially supported by a grant from the ECF and EPD of the Hong Kong Special Administrative Region, China (Project No. PolyU ECF111/2020).

## REFERENCES

- [1] Giancarlo Alfonsi. “Reynolds-Averaged Navier–Stokes Equations for Turbulence Modeling”. In: *Applied Mechanics Reviews* 62.4 (June 2009), p. 040802.
- [2] J Bogner et al. “Waste management in climate change 2007: Mitigation. contribution of working group iii to the fourth assessment report of the intergovernmental panel on climate change”. In: *Cambridge University Press, Cambridge* (2007).
- [3] Jason Brazile et al. “Toward scene-based retrieval of spectral response functions for hyperspectral imagers using Fraunhofer features”. In: *Canadian Journal of Remote Sensing* 34.sup1 (2008), S43–S58.
- [4] David Brüggemann et al. “Exploring relational context for multi-task dense prediction”. In: *Proceedings of the IEEE/CVF international conference on computer vision*. 2021, pp. 15869–15878.
- [5] Josep G Canadell et al. *Global carbon and other biogeochemical cycles and feedbacks*. 2021.
- [6] TV Chagovets, AV Gordeev, and L Skrbek. “Effective kinematic viscosity of turbulent He II”. In: *Physical Review E* 76.2 (2007), p. 027301.
- [7] Liang-Chieh Chen et al. “DeepLab: Semantic image segmentation with deep convolutional nets, atrous convolution, and fully connected crfs”. In: *IEEE transactions on pattern analysis and machine intelligence* 40.4 (2017), pp. 834–848.
- [8] Sergio Cogliati et al. “The PRISMA imaging spectroscopy mission: Overview and first performance analysis”. In: *Remote Sensing of Environment* 262 (2021), p. 112499.
- [9] J Andrzej Domaradzki and Eileen M Saiki. “A subgrid-scale model based on the estimation of unresolved scales of turbulence”. In: *Physics of Fluids* 9.7 (1997), pp. 2148–2164.

- [10] Markus D Foote et al. “Fast and accurate retrieval of methane concentration from imaging spectrometer data using sparsity prior”. In: *IEEE Transactions on Geoscience and Remote Sensing* 58.9 (2020), pp. 6480–6492.
- [11] Markus D Foote et al. “Impact of scene-specific enhancement spectra on matched filter greenhouse gas retrievals from imaging spectroscopy”. In: *Remote Sensing of Environment* 264 (2021), p. 112574.
- [12] Martin Hermann Paul Fuchs and Begüm Demir. “Hyspecnet-11k: A large-scale hyperspectral dataset for benchmarking learning-based hyperspectral image compression methods”. In: *IGARSS 2023-2023 IEEE International Geoscience and Remote Sensing Symposium*. IEEE. 2023, pp. 1779–1782.
- [13] Christopher C Funk et al. “Clustering to improve matched filter detection of weak gas plumes in hyperspectral thermal imagery”. In: *IEEE transactions on geoscience and remote sensing* 39.7 (2001), pp. 1410–1420.
- [14] Massimo Germano et al. “A dynamic subgrid-scale eddy viscosity model”. In: *Physics of Fluids A: Fluid Dynamics* 3.7 (1991), pp. 1760–1765.
- [15] Joseph Yossi Gil and Ron Kimmel. “Efficient dilation, erosion, opening, and closing algorithms”. In: *IEEE Transactions on Pattern Analysis and Machine Intelligence* 24.12 (2002), pp. 1606–1617.
- [16] Javier Gorroño et al. “Understanding the potential of Sentinel-2 for monitoring methane point emissions”. In: *Atmospheric Measurement Techniques* 16.1 (2023), pp. 89–107.
- [17] Robert O Green. “Spectral calibration requirement for Earth-looking imaging spectrometers in the solar-reflected spectrum”. In: *Applied optics* 37.4 (1998), pp. 683–690.
- [18] Luis Guanter et al. “Mapping methane point emissions with the PRISMA spaceborne imaging spectrometer”. In: *Remote Sensing of Environment* 265 (2021), p. 112671.
- [19] Kaiming He et al. “Deep residual learning for image recognition”. In: *Proceedings of the IEEE conference on computer vision and pattern recognition*. 2016, pp. 770–778.
- [20] Kaiming He et al. “Mask r-cnn”. In: *Proceedings of the IEEE international conference on computer vision*. 2017, pp. 2961–2969.
- [21] Kaiming He et al. “Spatial pyramid pooling in deep convolutional networks for visual recognition”. In: *IEEE transactions on pattern analysis and machine intelligence* 37.9 (2015), pp. 1904–1916.
- [22] Kun He et al. “Hashing as tie-aware learning to rank”. In: *Proceedings of the IEEE Conference on Computer Vision and Pattern Recognition*. 2018, pp. 4023–4032.
- [23] Zhiyi He et al. *UB-FineNet: Urban Building Fine-grained Classification Network for Open-access Satellite Images*. 2024. arXiv: 2403.02132 [cs.CV]. URL: <https://arxiv.org/abs/2403.02132>.
- [24] A Iravanian and Sh O Ravari. “Types of contamination in landfills and effects on the environment: a review study”. In: *IOP Conference Series: Earth and Environmental Science*. Vol. 614. 1. IOP Publishing. 2020, p. 012083.
- [25] Shaocheng Jia and Wei Yao. “Joint learning of frequency and spatial domains for dense image prediction”. In: *ISPRS Journal of Photogrammetry and Remote Sensing* 195 (2023), pp. 14–28. ISSN: 0924-2716.
- [26] Shenlu Jiang et al. “An Optimized Deep Neural Network Detecting Small and Narrow Rectangular Objects in Google Earth Images”. In: *IEEE Journal of Selected Topics in Applied Earth Observations and Remote Sensing* 13 (2020), pp. 1068–1081. DOI: 10.1109/JSTARS.2020.2975606.
- [27] Shenlu Jiang et al. “Space-to-speed architecture supporting acceleration on VHR image processing”. In: *ISPRS Journal of Photogrammetry and Remote Sensing* 198 (2023), pp. 30–44. ISSN: 0924-2716.
- [28] Siraput Jongaramrungruang et al. “MethaNet—An AI-driven approach to quantifying methane point-source emission from high-resolution 2-D plume imagery”. In: *Remote Sensing of Environment* 269 (2022), p. 112809.
- [29] Brian Edward Launder, G Jr Reece, and W Rodi. “Progress in the development of a Reynolds-stress turbulence closure”. In: *Journal of fluid mechanics* 68.3 (1975), pp. 537–566.
- [30] Min Lin, Qiang Chen, and Shuicheng Yan. “Network In Network”. In: *arXiv e-prints* (2013), arXiv-1312.
- [31] Shikun Liu, Edward Johns, and Andrew J Davison. “End-to-end multi-task learning with attention”. In: *Proceedings of the IEEE/CVF conference on computer vision and pattern recognition*. 2019, pp. 1871–1880.
- [32] Jonathan Long, Evan Shelhamer, and Trevor Darrell. “Fully convolutional networks for semantic segmentation”. In: *Proceedings of the IEEE conference on computer vision and pattern recognition*. 2015, pp. 3431–3440.
- [33] Cosimo Magazzino, Marco Mele, and Nicolas Schneider. “The relationship between municipal solid waste and greenhouse gas emissions: Evidence from Switzerland”. In: *Waste Management* 113 (2020), pp. 508–520.
- [34] Björn Maronga et al. “The Parallelized Large-Eddy Simulation Model (PALM) version 4.0 for atmospheric and oceanic flows: model formulation, recent developments, and future perspectives”. In: *Geoscientific Model Development* 8.8 (2015), pp. 2515–2551.
- [35] Ulrich Platt et al. *Differential absorption spectroscopy*. Springer, 2008.
- [36] Przemyslaw Polewski et al. “Instance segmentation of fallen trees in aerial color infrared imagery using active multi-contour evolution with fully convolutional network-based intensity priors”. In: *ISPRS Journal of Photogrammetry and Remote Sensing* 178 (2021), pp. 297–313.
- [37] Stephen B Pope. “Turbulent flows”. In: *Measurement Science and Technology* 12.11 (2001), pp. 2020–2021.

- [38] Siegfried Raasch and Michael Sch. “PALM-A large-eddy simulation model performing on massively parallel computers”. In: *Meteorologische Zeitschrift* 10.5 (2001), pp. 363–372.
- [39] Maithra Raghu. “On the expressive power of deep neural networks”. In: (2016).
- [40] Olaf Ronneberger, Philipp Fischer, and Thomas Brox. “U-net: Convolutional networks for biomedical image segmentation”. In: *Medical Image Computing and Computer-Assisted Intervention—MICCAI 2015: 18th International Conference, Munich, Germany, October 5-9, 2015, Proceedings, Part III* 18. Springer. 2015, pp. 234–241.
- [41] Pierre Sagaut and Yu-Tai Lee. “Large eddy simulation for incompressible flows: An introduction. scientific computation series”. In: *Appl. Mech. Rev.* 55.6 (2002), B115–B116.
- [42] Abubakar Sani-Mohammed, Wei Yao, and Marco Heurich. “Instance segmentation of standing dead trees in dense forest from aerial imagery using deep learning”. In: *ISPRS Open Journal of Photogrammetry and Remote Sensing* 6 (2022), p. 100024. ISSN: 2667-3932.
- [43] Muhammad Shafiq and Zhaoquan Gu. “Deep residual learning for image recognition: a survey”. In: *Applied Sciences* 12.18 (2022), p. 8972.
- [44] Jacquelyn Shelton, Przemyslaw Polewski, and Wei Yao. “U-Net for Learning and Inference of Dense Representation of Multiple Air Pollutants from Satellite Imagery”. In: *Proceedings of the 10th International Conference on Climate Informatics*. CI2020. virtual, United Kingdom: Association for Computing Machinery, 2021, pp. 128–133. ISBN: 9781450388481.
- [45] Thomas F Stocker et al. “Technical summary”. In: *Climate change 2013: the physical science basis. Contribution of Working Group I to the Fifth Assessment Report of the Intergovernmental Panel on Climate Change*. Cambridge University Press, 2013, pp. 33–115.
- [46] Juan Terven and Diana Cordova-Esparza. “A comprehensive review of YOLO: From YOLOv1 to YOLOv8 and beyond”. In: *arXiv preprint arXiv:2304.00501* (2023).
- [47] James Theiler and Bernard R Foy. “Effect of signal contamination in matched-filter detection of the signal on a cluttered background”. In: *IEEE Geoscience and Remote Sensing Letters* 3.1 (2006), pp. 98–102.
- [48] David R Thompson et al. “Atmospheric correction for global mapping spectroscopy: ATREM advances for the HypIRI preparatory campaign”. In: *Remote Sensing of Environment* 167 (2015), pp. 64–77.
- [49] Andrew K Thorpe et al. “Airborne DOAS retrievals of methane, carbon dioxide, and water vapor concentrations at high spatial resolution: application to AVIRIS-NG”. In: *Atmospheric Measurement Techniques* 10.10 (2017), pp. 3833–3850.
- [50] Andrew K Thorpe et al. “High resolution mapping of methane emissions from marine and terrestrial sources using a Cluster-Tuned Matched Filter technique and imaging spectrometry”. In: *Remote Sensing of Environment* 134 (2013), pp. 305–318.
- [51] Daniel J Varon et al. “Quantifying methane point sources from fine-scale satellite observations of atmospheric methane plumes”. In: *Atmospheric Measurement Techniques* 11.10 (2018), pp. 5673–5686.
- [52] Andreas Veit, Michael J Wilber, and Serge Belongie. “Residual networks behave like ensembles of relatively shallow networks”. In: *Advances in neural information processing systems* 29 (2016).
- [53] T Wagner et al. “MAX-DOAS O4 measurements: A new technique to derive information on atmospheric aerosols—Principles and information content”. In: *Journal of Geophysical Research: Atmospheres* 109.D22 (2004).
- [54] Xinlong Wang et al. “Solov2: Dynamic and fast instance segmentation”. In: *Advances in Neural information processing systems* 33 (2020), pp. 17721–17732.
- [55] Zhiming Yang, Shigemi Kagawa, and Jing Li. “Do greenhouse gas emissions drive extreme weather conditions at the city level in China? Evidence from spatial effects analysis”. In: *Urban Climate* 37 (2021), p. 100812.
- [56] Ning Zang et al. “Land-use mapping for high-spatial resolution remote sensing image via deep learning: A review”. In: *IEEE Journal of Selected Topics in Applied Earth Observations and Remote Sensing* 14 (2021), pp. 5372–5391.
- [57] Chengliang Zhang et al. “Greenhouse gas emissions from landfills: A review and bibliometric analysis”. In: *Sustainability* 11.8 (2019), p. 2282.
- [58] Lichen Zhou, Chuang Zhang, and Ming Wu. “D-LinkNet: LinkNet with pretrained encoder and dilated convolution for high resolution satellite imagery road extraction”. In: *Proceedings of the IEEE conference on computer vision and pattern recognition workshops*. 2018, pp. 182–186.